A prediction model of failure threshold for shear deformation in a Zr-based bulk metallic glass

H.R. Cheng[1], Z. Wang[2,*], J. Brechtl[3], W. Wen[4], M. Zhang[1], Z.H. Wang[2], J.W. Qiao[1,]**

[1]College of Materials Science and Engineering, Taiyuan University of Technology, Taiyuan 030024, China

[2]Institute of Applied Mechanics, College of Aeronautics and Astronautics, Taiyuan University of Technology, Taiyuan 030024, China

[3]Oak Ridge National Laboratory, Oak Ridge, TN 37831, USA

[4]School of Engineering, Lancaster University, LA1 4YW, UK

Abstract

The failure of bulk metallic glasses (BMGs) during plastic deformation at room temperature is abrupt and instantaneous, while the analysis of precursor information based on avalanche events helps predict catastrophic failure. Acoustic emission (AE) signal can provide accurate precursor information for material failure, due to its sensitive and high fast calculation ability. In the current study, AE monitoring tests are carried out during uniaxial compression tests of BMGs at different strain rates. The AE experimental failure threshold, E_{max}, is proposed on the basis of AE cumulative energy, which reflects the intensity of damage evolution at different loading conditions. Compared with the critical shear band velocity (CSBV) associated with stick-slip dynamics of serrated flow, E_{max} is a more sensitive failure parameter since it is connected with the local microscopic events changes in the material response process. Here, the E_{max} is obtained prior to CSBV since the calculation of these two avalanches

analysis focuses on the different stages of shear band growth. In particular, AE events are related to the “dry” friction process in the first stage, however, the CSBV is responsible for the “viscous” glide in the second stage. Therefore, E_{max} is not affected by the complex interaction between the shear bands in the stick-slip process. The maximum avalanche of serrated flow, S_{max}, is proposed as the experimental failure threshold, which depends on the applied strain rates as $S_{max} \sim \dot{\varepsilon}^{-\lambda}$. According to the relationship of E_{max} and S_{max}, the theoretical failure threshold, E_{max}, follows a criterion $E_{max} = 2545\dot{\varepsilon}^{-\lambda} - 4468$, where λ is equivalent to 0.15 for this work. Combining the different calculations and AE measurements, this model gives new insights to predict the deformation failure behavior of the Zr-based BMGs.

Keywords: Bulk metallic glasses; Failure threshold, Shear deformation; Acoustic emission; Real-time monitor

Corresponding authors: Z. Wang Email: zhongwangty@hotmail.com
J.W. Qiao Email: qiaojunwei@gmail.com

1. Introduction

Metallic glasses (MGs) have received extensive attention from the basic and applied research communities since being discovered in the 1960s [1] due to their unique material properties [2]. The emergence of bulk metallic glasses (BMGs) is considered to be a milestone because they display unique and intriguing mechanical, chemical, and physical properties [3-5]. Furthermore, more interesting properties have been discovered due to significant progress in alloy development over the past few decades [6, 7]. Nevertheless, a serious factor limiting structural application is their poor macroscopic plasticity at ambient temperature [4, 8]. After the BMGs yield at room temperature shear bands rapidly form and propagate, leading to plasticity being produced via highly localized shear bands [9].

Avalanche events (such as serrated flow and acoustic emission) caused by shear bands serve as a bridge between the macroscopic plasticity and the shear process of BMGs. Dynamics analysis of a series of avalanche events helps predict and monitor such catastrophic failures [10, 11]. For example, Qiao et al. [12] predicted the maximum stress drop associated with the avalanche size of plastic instability events, which can be used as a criterion of the material before failure. Furthermore, combined with the mean-field model, a simpler and more effective theoretical failure threshold model directly related to the glass transition temperature of the BMGs was established [13]. Such a finding was helpful in better understanding the unpredictable catastrophic failure of BMGs at room temperature. However, these prediction methods do not provide a way to respond to the instability and failure of materials during mechanical

testing since they cannot directly capture the serration size during plastic deformation. Thus, the stress drop (S) needs to be calculated indirectly by processing the stress-strain (time) curves.

The second type of experimental method for studying avalanches is based on the measurement of local microscopic events related to the material response process [14]. For example, acoustic emission (AE) technology is applied to monitor transient elastic waves in solids due to rapid and local structural changes. This technology has been widely used in mine safety monitoring [15, 16]. For instance, when the material is close to the final damage event AE activity will increase significantly, which is a "warning signal" for imminent material failure [15]. The moment when the AE activity suddenly changed was regarded as the critical point of specimen instability [16, 17]. In a study by Zhang et al. [18], which examined the precursory early warning information of AE parameters during the uniaxial compression of tuffs, found that the AE cumulative energy changed from a slow, progressive rise to an instantaneously significant increase before failure. This turning point has been treated as a precursor time point used for the prediction of rock failure [17, 18]. Although a variety of theoretical frameworks [19-21] have been used to analyze and predict the burst sizes of serrated flow in BMGs, predicting burst sizes of AE related to the shear bands is still poorly understood. In this paper, we will estimate the largest burst sizes of AE by relating the experimental failure threshold of serrated flow, S_{max}, with the experimental failure threshold of AE energy, E_{max}, during plastic deformation in BMGs.

2. Experimental procedures

Alloy ingots with a nominal composition of $Zr_{52.5}Cu_{17.9}Ni_{14.6}Al_{10}Ti_5$ (Vit105) were prepared by induction melting high purity (purity>99.9%) constituents in a Ti-gettered argon atmosphere, followed by suction casting to form rods with a diameter of 2 mm. Compressive testing specimens of 5 mm in height were cut from as-cast rods by means of a diamond saw using cutting fluid as a coolant. The cut samples were then ground and polished to 4 mm (aspect ratio of 2:1). Compression tests were carried out using an Instron 5969 machine, and the data acquisition rate is 100 Hz. The samples were tested using strain rates of 3×10^{-3}, 3×10^{-4}, and 3×10^{-5} s^{-1} at room temperature. A computer-controlled DS5 device was used to monitor the AE activity during the compression tests. The RS-35C sensor with a flat response in the 100 - 600 kHz frequency band ensures good acoustic contact by using vacuum grease. The preamplifier gives a gain of 40 dB.

3. Results

3.1. AE amplitude

The compressive stress curves and AE amplitude spectrum at different strain rates (3×10^{-3}, 3×10^{-4}, and 3×10^{-5} s^{-1}) are exhibited in Figs. 1(a), 1(c), and 1(e). Based on the high time resolution of AE, the stress-time curve is plotted to synchronize the two experimental processes. In BMGs, serrated flow is often observed at low strain rates during inhomogeneous deformation [22, 23], which typically manifests as a repeated cycle of sudden stress drops and subsequent elastic reloading. Stress drop

behavior is commonly used to study avalanche events, which reflects the whole process from shear band nucleation to arrest [24]. AE measurement represents a unique method that is used to monitor the local irreversible stress relaxation process at the source in real-time [25], which cannot be obtained by other means with the same time resolution. Therefore, during inhomogeneous plastic flow shear bands act as a strong AE source [26, 27]. Here, AE signals are concentrated during the process of inhomogeneous plastic flow. A small number of AE signals observed below the macroscopic yield point can be attributed to the initiation and propagation of shear bands [28]. The local amplification diagram is displayed in Figs. 1(b), 1(d), and 1(f) for strain rates of 3×10^{-3}, 3×10^{-4}, and 3×10^{-5} s^{-1}, respectively, which shows that an AE burst is related to the onset of a stress drop. In the later stage of plastic deformation, the amplitude of AE increases as a whole, and the frequency of large-scale signals increases significantly. Thus, the intensity of AE events is expected to characterize the steady state of shear band growth. However, the AE amplitude is the maximum (peak) value that a waveform attains, which misses the duration of the micro-events change. The AE energy is calculated by integrating the envelope area of the entire waveform, which better reflects the intensity of micro-events change [14]. Therefore, the AE energy is chosen as a parameter for the subsequent study of avalanche events.

Consistent with previous reports [26, 29], most of the AE bursts always occur near the beginning of the stress drop. This phenomenon is because the shear band growth is a dynamic process where the first stage is related to “dry” friction in which AE is produced more readily [29], and the second stage is related to “viscous” glide,

manifested as a stress drop. Therefore, AE technology is expected to preferentially reflect the precursor information of BMGs failure. The moment when the AE activity suddenly changes can be regarded as the AE critical point of BMG failure. Based on the "viscous" glide in the second stage of shear band growth, Sun et al. [30] calculated the instantaneous velocity of the shear band sliding process and found that when the instantaneous velocity reached the critical shear band velocity (CSBV) catastrophic failure occurred. The CSBV of the serration is expected to be located later than the AE critical point since it is calculated based on the macroscopic changes of the system, which may be the result of the overlap of many continuous microscopic events.

3.2. AE energy

The stress-time curves, AE energy, and AE cumulative energy for different strain rates are shown in Figs. 2(a), 2(b), and 2(c). The AE energy release can predict the generation of damage within the material, and the AE cumulative energy can reflect the intensity of damage evolution at different loading stages [31]. During the compression test, the elastic regime is characterized by a lack of AE events and energy readings. However, AE events begin to be detected as the stress-time curve approaches the macroscopic yield point, which is accompanied by an increase in the AE cumulative energy. Thus, the appearance of the AE cumulative energy curve can be regarded as the beginning of the plastic deformation stage. At a strain rate of 3×10^{-3} s^{-1}, the propagation of the shear band is a large avalanche-induced mode [24, 32] in which the shear band, propagating simultaneously, is unstable. Thus, a decrease in the number of low energy events (energy < 100 mV·ms) is accompanied by an increase in the number

of medium (100 mV·ms < energy < 1000 mV·ms) and high (energy > 1000 mV·ms) energy events, resulting in the rapid increase in the AE cumulative energy curve. For the other strain rates, the propagation mechanism of the shear band belongs to a small avalanche-mediated mode [32, 33] in which the plastic deformation is more stable. After yielding, the AE energy signal is characterized by a larger number of low and medium energy events such that the AE cumulative energy curve increases more smoothly. As for the late deformation stage, the frequency of the large energy events increased significantly for all three strain rates. Therefore, the AE cumulative energy increases sharply until it reaches a “turning point”, which corresponds to the position with the largest slope on the AE cumulative energy curve. This observed “turning point” may correspond to a severe atomic activation event occurred during shear band growth that is characteristic of a large-scale AE event.

Such a turning point also occurs in other brittle materials, such as tuffs, which is regarded as a “critical damage precursor point” [18]. Such a finding suggests that in this type of sudden change in the AE cumulative energy is also a precursory feature of failure in BMGs, which is expected to be considered a "precursor point". Usually, the "precursor point" corresponds to the maximum energy ($E_{\max}$) before failure, and $E_{\max}$ shows power law related to the strain rate such that it satisfies $E_{max} \sim \dot{\varepsilon}^{-\lambda}$, as illustrated in Fig. 2(d). Similar to the maximum stress drop ($S_{\max}$) increases quite significantly with decreasing strain rate, due to the linear relationship between the increment of free volume and strain rates [13, 34].

4. Discussion

4.1. The critical shear-band velocity

The analysis of the stress-time curves and the AE signal spectrum above as shown in Fig. 2, indicates that the evolution process of the two types of avalanches (serration and AE) is highly correlated with the deformation and failure process. Maximum-scale avalanches (S_{max} and E_{max}) tend to occur before the fracture of BMGs. To further elucidate the effectiveness of the AE "precursor point", CSBV, which is directly related to the steady state of the shear band, is considered for comparison.

Existing studies generally consider that [35-37] the serration behavior occurring in BMGs is mainly caused by the intermittent sliding or the stick-slip process. Based on this theory, Sun et al. [30] simplified the shear band motion using a stick-slip model and used the stick-slip dynamics of a single primary shear band to measure the shear band velocity (SBV). During the compression process, the operation of the shear band will cause the release of the elastic energy stored in the machine-sample system, thereby partially relaxing the compressive load [30].

Assuming that a load P is initiated at time $t = 0$, the stress $\sigma = 4P/\pi D^2$ applied to a cylindrical sample with a diameter of D at time t can be expressed as [38, 39]:

$$\sigma = k(v_0 t - x) = k(v_0 t - \int_0^t v \mathrm{d}\tau) \quad (1)$$

where $k = E/L(1+S)$ is the elastic constant of the machine-sample system for the cylindrical sample [39] (E and L are the Young's modulus and sample length, respectively), S is the ratio of the sample stiffness κ_S to the machine stiffness κ_M and is also equivalent to the expression $\pi D^2 E/(4L\kappa_M)$, v_0 is the loading velocity, and x is the

vertical displacement caused by shear band slip. Furthermore, v is the instantaneous SBV that is obtained by differentiating equation (1) with respect to time *t*, which gives:

$$v = v_0 - \frac{1}{k}\frac{d\sigma}{dt} \tag{2}$$

According to equation (2), as long as the derivative of the loading stress with time could be experimentally resolved, the time dependent SBV profile for a shear band can be calculated. The stress-time and stress derivative-time curves for a strain rate of 3×10^{-5} s^{-1} are displayed in Fig. 3(a). At the initial stage of yielding, there are many dense, small fluctuations between the intervals of the derivative curves, and these small serrations often occur between the relatively large serrations. In the later stage of plastic deformation, the serrated flow is characterized by large serrations that occur periodically, resulting in a derivative curve which exhibits periodic fluctuations. The time distribution of SBV, as calculated by equation (2), is displayed in Fig. 3(b), which demonstrates that the shear band velocity increases rapidly to the maximum and then decreases rapidly to zero from the beginning of the slip. Subsequently, a similar process occurs until the next sliding event is triggered, which conforms to the typical stick-slip dynamic behavior.

For each slip event, a maximum shear band velocity (MSBV) is obtained. The overall distribution of the MSBV during a single experiment is plotted in Fig. 3(c). For all three strain rates, a maximum MSBV appears during the later stage of deformation. Due to the short duration of the final fracture process, it is difficult to accurately determine the CSBV at the time of crack formation. Therefore, among all the detectable MSBVs, the maximum MSBV is selected as the CSBV, which is close

to a constant value of $(1.5 \pm 0.4) \times 10^{-4}$ m/s no matter how the internal and external conditions change [30]. When the shear band velocity reaches the CSBV, catastrophic failure will be triggered.

4.2. The lag of CSBV appearance

The positions of the two critical points on the stress-time curve at different strain rates (3×10^{-3}, 3×10^{-4}, and 3×10^{-5} s^{-1}) are exhibited in Figs. 3(d), 3(e), and 3(f), from which the data points represent the derivative of the increase process of the AE cumulative energy curves, and the AE critical point E_{max} corresponds to the data point with the maximum derivative while the CSBV is represented by a red dotted line. Comparing the two critical points, their positions are close. Table 1 lists the corresponding positions of the two critical points on the stress-strain curve. It can be found that the difference between the two critical points at three strain rates is within 1 % of the strain range. This behavior is especially apparent at 3×10^{-3} s^{-1} where the two critical points deviate only one serration event. AE measurement captures the transient elastic waves in solids due to rapid and local structural changes, making it very sensitive to short-term microscopic changes [14] and corresponds to the first stage of shear band growth [29]. Instead, the serrated flow by force measurement reflects the macroscopic changes of the system [14] and is the performance of the second stage stick-slip motion. The macroscopic changes may be the result of the overlap of many continuous microscopic events, which makes CSBV always occur after the AE critical point.

For ductile BMGs, multiple shear bands are generated under proper loading conditions [40, 41]. Meanwhile, in samples with better plasticity shear band interactions are more obvious [41, 42]. Although the final state of the unstable expansion of the sample along the main shear band cannot be changed, the appearance of multiple shear bands and the strong interaction between the shear bands delay the propagation of the primary shear band [41, 43]. Furthermore, the strong interaction between shear bands dissipates the energy of the primary shear band expansion to a certain extent [44, 45]. During the process of stable deformation, the stored energy is easily dissipated by the slip of the shear band, which is manifested as a mixed occurrence of large and small serrations such that the shear band velocity is relatively stable. Furthermore, greater shear slip is required to dissipate energy near failure, which manifests as large periodic serrations [46]. The MSBV, as shown in Fig. 3(c), increases significantly near failure, which means that the shear band becomes unstable. The above results indicate that the shear band velocity is directly related to the stable state of the shear band through the macroscopic serration. Therefore, the critical point for the CSBV that is calculated based on the stick-slip dynamic model is always closer to the point of fracture. On the contrary, AE events are related to the first stage of “dry” friction [29] of shear band growth and are not affected by the complex interaction between shear bands during sliding, which implies that a more sensitive material failure reference is acquired from AE events.

4.3. Damage characteristics based on AE

As mentioned above, the change in the AE signal is related to the shear band activity. Therefore, the intrinsic relationship between AE activity and material deformation can be used to measure damage [31]. AE damage characterization can be used to assess the stability of shear zones. Furthermore, the AE cumulative energy can be used as a damage metric [47] to analyze the damage evolution characteristics. The AE cumulative energy curves for different strain rates (3×10^{-3}, 3×10^{-4}, and 3×10^{-5} s^{-1}) are displayed in Fig. 4(a). Here, the evolution trends are similar, where they rise slowly in the elastic stage and then increase exponentially after yielding. The exponential relationship between the AE cumulative energy and time is given as [31]:

$$W = ae^{bt} + c \tag{3}$$

where a, b, and c are fitting parameters, as plotted in Fig. 4(a). The damage variable D was first proposed by a Soviet scholar Kachanov [48], which is a measure of the degree of deterioration of materials or structures. The damage variable D is defined as:

$$D = \frac{N_d}{N} \tag{4}$$

where N_d is all the area of the micro-defects on the bearing section and N is the initial non-destructive area. If the AE cumulative energy, at the moment when the non-destructive cross-sectional area completely loses the bearing capacity is defined as E_0, the AE cumulative energy per unit area of the sample E_w is calculated as [47]:

$$E_w = \frac{E_0}{N} \tag{5}$$

When the cross-sectional area of the damage is equal to N_d, the AE cumulative energy, E_d, is:

$$E_d = E_w N_d = \frac{E_0}{\mathrm{N}} N_d \tag{6}$$

Thus, the damage based on the AE cumulative energy is expressed as:

$$D_{\mathrm{E}} = \frac{E_{\mathrm{d}}}{E_{0}} \tag{7}$$

The relationship between the normalized strain and the damage coefficient D_{E} is plotted in Fig. 4(b). The results reveal that the damage variable D_{E} correlates well with the normalized strain. The plot is divided into three stages, flat, slow, and rapid growth. The flat D_{E} curve indicates that the sample is still in the elastic stage. Since the shear band is the source of the AE signal [26, 27], the slow increase of D_{E} indicates that the sample is in a stable plastic deformation stage. While for high strain rates (3×10^{-3} s^{-1}), the plastic flow of the sample is unstable [49], resulting in the rapid increase of D_{E} after sample yielding. It is reported that for brittle materials such as sandstones [31], the rapid increase of D_{E} means that the sample has entered the yield stage, and the turning point of D_{E} corresponds to the yield threshold of the material. In BMGs, the rapid increase of D_{E} indicates that the sample enters the unstable plastic deformation stage, indicating that the turning point of D_{E} corresponds to the end of the stable plastic deformation stage in this material. Thus, the maximum AE energy observed during the rapid increase stage of D_{E} is an indicator of the “precursor point” of material failure.

4.4. Probability distribution functions

The statistical analysis of avalanche events reveals the mechanical response mechanism and physical characteristics of the studied system [50, 51]. In particular, previous statistical analysis of BMGs mainly focused on serrated flow. For example, the serrated flow dynamics shift from peak value to power law behavior with the change of strain rate [40, 52]. Meanwhile, the evolution of shear banding with a power law

distribution is stable, resulting in larger plasticity [53]. The statistical analysis is also used in studies where avalanche patterns manifest as AE. For example, the statistics of AE energy or durations reveals a power law distribution, which indicates that the system evolves in a dynamic critical state [14, 51]. The probability distribution function (PDF) is defined as the number of events in a given energy range divided by the total number of events, which requires artificially dividing the energy interval and requiring the sample with a good power law behavior to avoid affecting the statistical results of the power law exponent [54]. For ductile BMGs, the existence of multiple shear bands plays a significant role in the formation of plastic deformation and a self-organized critical state, which results in serration event sizes that follow a power-law distribution [41, 55]. Therefore, a strain rate of $3 \times 10^{-4}\ s^{-1}$ that results in plastic deformation with strong shear band interactions, is selected for AE avalanche statistical analysis. In the double logarithmic coordinates, the AE energy follows the power law, $P(E) \sim E^{-\varepsilon}$, as observed in Fig. 5(a). The slope of the power law line is the exponent controlling this distribution, which is around 1.54. This result is similar to sandstone which has an energy exponent between 1.44 and 1.55 [56]. In fact, the results of AE experiments have shown that the spatial distribution of microcracks in sandstone is similar to that of shear band nucleation sites in BMGs [15]. In the early stage of compression, the AE of avalanches distribute randomly. During loading, the main damage zone that forms has an orientation of about 45° along the loading direction. Furthermore, this power law exponent is close to the value obtained using mean field theory [50, 57]. The mean field theory points out that the avalanche is caused by the local shear stress of the weak point

exceeding the random local sliding threshold, resulting in the sliding of this point. Through the elastic interaction the sliding weak point may cause other ones to slide, resulting in a sliding avalanche [21]. For BMGs, the weak point may consist of shear transformation zones (STZs) [49], which is a collective rearrangement of 10-100 atoms [4].

Macroscopically, the BMGs deform plastically resulting in serrated flow, whereas the changes in micro events are manifested through AE events [14]. As mentioned above, the AE event corresponds to the first “dry” friction stage of the shear band activity, which covers the process of STZ atomic rearrangement. Therefore, the AE energy exponent is close to the value obtained from the mean field theory. This result also verifies that inhomogeneous deformation of BMGs is carried out by the sliding avalanche of STZs from the experimental point of view. At the same time, the power law distribution means that the system evolves in a dynamic critical state [51]. The power law exponents of some other brittle materials are listed in Table 2. Here, materials such as coal exhibit a significantly lower exponent than that of other brittle materials, which is due to the material structure [47].

In porous materials, the PDF reflects the different damage stages that occur inside the material during deformation [16, 58]. For example, Salje et al. [59] pointed out that the critical exponent reflected the damage statistics in sandstone during creep, and the critical exponent of the whole process was the superposition of different sub-stages. In BMGs, the AE event is generated synchronously with the serrated flow. However, high-energy events are not only observed near failure. By investigating the

contribution of AE energy at different magnitudes to power law behavior, a comprehensive analysis of AE events can be achieved. The probability distribution of AE events of different magnitudes is shown in Fig. 5(b), in which AE events are divided into three types: high, medium, and low energy. Here, the power law exponent of the medium energy events is close to the exponent of entire AE energy sets, which indicates that medium energy events primarily contribute to the main power law behavior. Although the high and low energy events present power law behavior, they reflect different power law exponents. The shallow power law exponent means that the frequency distribution of events in each interval is more uniform. In other words, the distribution is characteristically more uniform with respect to the whole deformation process, which is not a sign of triggering catastrophic failure. The high energy events correspond to a large exponent, which indicates that the probability distribution for events within a given range is more skewed and the occurrence of events is more rapid such that a sudden occurrence will trigger catastrophic damage. Therefore, it is reasonable to choose E_{max} from high energy events as a precursor of damage.

The AE duration refers to the time interval from the first time the signal crosses the threshold to the final time in which it drops back to the threshold. The PDF of the AE duration is divided into three regions based on the distribution of different AE source durations (see Fig. 6). Different from the distribution of AE durations in crystalline alloys which is the dislocation motion as the source of AE. [60], the microstructure in BMGs is given by shear bands. The AE event signals with short durations (duration <600 μs) and long durations (duration >1500 μs) are concentrated

in regions I and III, respectively. Here, a part of the short events is observed in region I due to the influence of factors such as low-frequency vibrations of the instrument and acoustic echo. Whereas region III exhibits apparent power law behavior with an exponent of around 1.54, which was observed in Fig. 6. According to the definition of AE energy, $E = \frac{1}{R}\int_0^{\mathrm{D}} U^2(\mathrm{t})\mathrm{dt}$ [16], the duration is an important parameter when calculating the area covered by the signal detected, which may be the primary reason for similar power law exponents in these two AE parameters.

4.5. Theoretical failure threshold

As mentioned above, a more sensitive material failure metric is acquired from AE events based on the high sensitivity and efficient calculations of AE signal. Generally, the largest scale avalanche directly observed from experimental results is called the experimental failure threshold [13]. Although the experimental failure threshold of AE exhibits a power law behavior related to the strain rate, the significant variations in the experimental failure thresholds at different strain rates necessitate the establishment of a theoretical failure threshold that is correlated with strain rates.

The experimental failure threshold, $S_{\max}$, of serrated flow significantly decreases with an increase in the strain rate, and the following relationship with the strain rates is obtained as [13]:

$$S_{max} \sim \dot{\varepsilon}^{-\lambda} \tag{8}$$

where λ varies from about 0.1 to 0.22 [13, 49, 53, 61]. The fitted value of this work is 0.15, as shown in Fig. 7(a).

Both experimental failure thresholds (E_{max} and S_{max}) exhibit the power law behavior related to the strain rate due to the clear linear correlation between the increment of free volume and strain rates [13, 34]. Fig. 7(b) displays the correspondence between the two experimental failure thresholds at different strain rates, which shows an apparent linear correlation. The correlation between the two avalanche thresholds from Fig. 7(b) is expressed as:

$$E_{max} \sim bS_{max} - a \tag{9}$$

where b is the slope of the correlation curve and a is the intercept, expounded in Fig. 7(b).

Although the fitted value of a in equation (9) fluctuates significantly within the error range, it still needs to combine with the experimental values for correction. The slight difference in the position of sensors or the position of the AE source will cause the received signal to attenuate in varying degrees during the propagation of sound waves [62]. At low strain rates, larger-scale avalanches result in the more pronounced attenuation of sound waves. Consequently, the experimental failure threshold at low strain rates, E_{max}, exhibits a relatively wide range of values. The E_{max} at high strain rates is introduced into equation (9) as a theoretical failure threshold to obtain the constant a=4563. Substitution of equation (8) into equation (9) gives:

$$E_{max} = 2545\dot{\varepsilon}^{-\lambda} - 4468 \tag{10}$$

where λ is related to the maximum stress drop from equation (8). As previously mentioned, this value typically ranges between 0.1 and 0.22 and the fitted value of this experiment is 0.15.

A comparison between experimental values E_{max}, and theoretical expression is demonstrated in Fig. 8. At low strain rates, due to the influence of acoustic wave attenuation, the error bars of the experimental values are relatively larger and tend to be lower than the theoretical values. Overall, the experimental and predicted results are comparable.

In summary, AE experimental failure thresholds, E_{max}, at different strain rates (3×10^{-3}, 3×10^{-4}, and 3×10^{-5} s^{-1}) all preceded the critical points of serrated flow, which reflected the effectiveness of using AE signal for failure prediction. The output of AE measurements was influenced by many factors, for example, the sample size and geometry, which resulted in characteristics of AE parameter are not directly related to the change of the system [14]. Thus, in order to predict the theoretical failure threshold, E_{max}, the relationship between the maximum avalanche size measured by AE and stress drop (S_{max}), which express the macroscopic changes of the system, was established. Combined with the high sensitivity and efficient calculations of the AE signal, the AE burst sizes was obtained by AE software immediately during the compression tests. Thus, this method is useful in predicting the plastic deformation failure during mechanical testing.

5. Conclusions

(1) The AE amplitude and energy behavior were analyzed at different strain rates (3×10^{-3}, 3×10^{-4}, and 3×10^{-5} s^{-1}), and similar trends were obtained. The AE cumulative energy can reflect the intensity of damage evolution, which is used to identify the AE experimental failure threshold, E_{max}. When the cumulative energy

curve increases sharply, a “turning point” is observed, which corresponds to the position with the largest slope on the AE cumulative energy curve. This “turning point” usually corresponds to the AE experimental failure threshold, E_{max}, as a precursory feature of BMG failure.

(2) Compared with the critical points of serrated flow, AE experimental failure thresholds, E_{max}, all precede the CSBV for all strain rates, indicating that a more sensitive material failure threshold is acquired from AE events. Since the shear band growth is a dynamic process, the CSBV is related to the second stage of “viscous” glide. On the contrary, AE events are related to the first stage of “dry” friction of shear band growth and are not affected by the complex interaction between shear bands during sliding. At the same time, the macroscopic changes expressed by serrated flow occurring during the serrations may be the result of the overlap of many continuous microscopic events measured by AE.

(3) Energy is an important parameter of the AE signal, which can predict the damage generation in BMGs. The AE duration suggests a non-negligible contribution to the AE energy, which exhibits similar power law exponents with AE energy. The power law behavior observed in the PDF of the two parameters means that the system evolves in a dynamic critical state.

(4) Experimental failure thresholds (E_{max} and S_{max}) are power law related to the strain rate due to the clear linear correlation between the increment of free volume and strain rates. Based on the relationship between the maximum avalanche size (E_{max}) measured by AE and stress drop (S_{max}), the theoretical AE failure threshold, E_{max},

related to the strain rates is established. In this work, the largest AE burst sizes is predicted by $E_{\max} = 2545\dot{\varepsilon}^{-\lambda} - 4563$. Here, λ is the fitted value related to the maximum stress drop ($S_{\max}$), which is equivalent to 0.15 for the Vit105 BMG at ambient temperature. This formula can act as a criterion to predict the plastic deformation failure in tests. Such AE measurements provide us with an approach to monitor the stable state of shear bands during mechanical testing.

CRediT authorship contribution statement

H.R. Cheng: Methodology, Writing – original draft. **Z. Wang:** Writing – review & editing, Supervision, Funding acquisition. **J. Brechtl:** Writing – review & editing. **W. Wen:** Data curation, Formal analysis. **M. Zhang:** Formal analysis, Supervision. **Z.H. Wang:** Investigation, Data curation. **J.W. Qiao:** Supervision, Funding acquisition.

Declaration of competing interest

The authors declare that they have no known competing financial interests or personal relationships that could have appeared to influence the work reported in this paper.

Data availability

Data will be made available on request.

Acknowledgments

The authors would like to acknowledge the financial support of the National Natural Science Foundation of China (Nos. 52201188, 52271110), the Natural Science

Foundation of Shanxi Province, China (No. 20210302124423), and the Research Project of Shanxi Scholarship Council of China (No. 2022–037).

FIGURE CAPTIONS

Fig. 1 Stress-time curves and AE amplitude spectrum at different strain rates ((a), (b) 3×10^{-3} s^{-1}; (c), (d) 3×10^{-4} s^{-1}; (e), (f) 3×10^{-5} s^{-1}).

Fig. 2 AE energy, cumulative energy curves, and stress-time curves at different strain rates ((a) 3×10^{-3} s^{-1}; (b) 3×10^{-4} s^{-1}; (c) 3×10^{-5} s^{-1}); (d) Variation of the E_{max}, vs strain rates. The relation, $E_{max} \sim \dot{\varepsilon}^{-\lambda}$, is obtained by fitting.

Fig. 3 (a) Stress-time and stress derivative-time curves for a strain rate of 3×10^{-5} s^{-1}; (b) Instantaneous shear band velocity; (c) The distribution of extracted MSBV with time for the SBV profile; Comparison of the positions of the two critical points on the stress-time curve at different strain rates ((d) 3×10^{-3} s^{-1}; (e) 3×10^{-4} s^{-1}; (f):3×10^{-5} s^{-1}).

Fig. 4 (a) AE cumulative energy curves at different strain rates; (b) Relationship between damage variable and normalized strain.

Fig. 5 (a) AE energy probability distribution; (b)The probability distribution of AE energy of different magnitude.

Fig. 6 Probability distribution of the AE duration.

Fig. 7 (a) Variation of the S_{max}, vs strain rates. The relation, $S_{max} \sim \dot{\varepsilon}^{-\lambda}$, is obtained by fitting; (b) The correspondence between E_{max} and S_{max}.

Fig. 8 The comparison between experimental values and theoretical formulas.

TABLE CAPTIONS

Table 1 The position of the critical point on the stress-strain curve.

Table 2 AE energy power law exponent statistics of some brittle materials.

Fig. 1

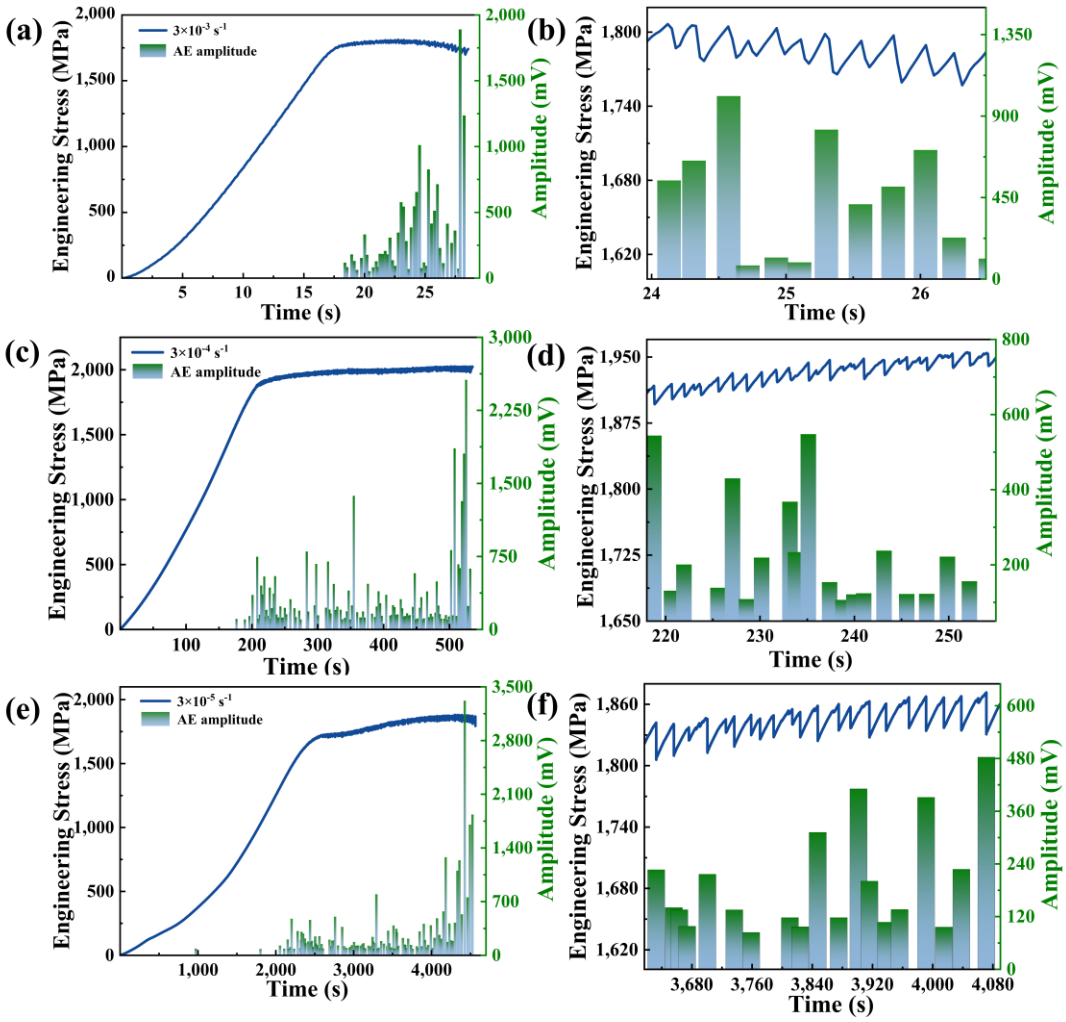
(a)
3×10⁻³ s⁻¹
AE amplitude
Engineering Stress (MPa)
Amplitude (mV)
Time (s)
(b)
Engineering Stress (MPa)
Amplitude (mV)
Time (s)
(c)
3×10⁻⁴ s⁻¹
AE amplitude
Engineering Stress (MPa)
Amplitude (mV)
Time (s)
(d)
Engineering Stress (MPa)
Amplitude (mV)
Time (s)
(e)
3×10⁻⁵ s⁻¹
AE amplitude
Engineering Stress (MPa)
Amplitude (mV)
Time (s)
(f)
Engineering Stress (MPa)
Amplitude (mV)
Time (s)

Fig. 2

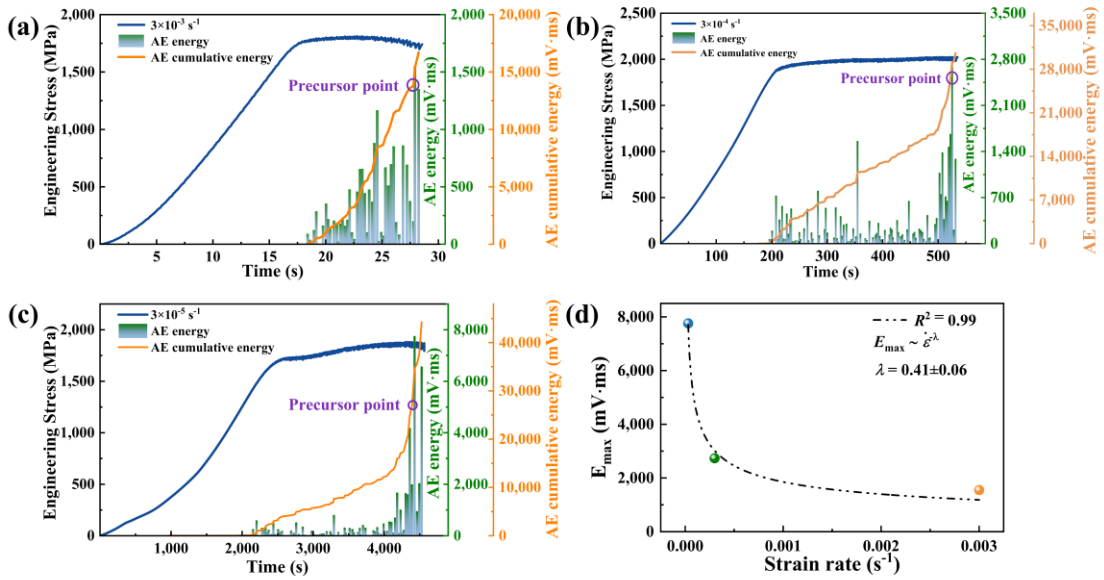
(a)
3×10⁻³ s⁻¹
AE energy
AE cumulative energy
Precursor point
Engineering Stress (MPa)
AE energy (mV·ms)
AE cumulative energy (mV·ms)
Time (s)
(b)
3×10⁻⁴ s⁻¹
AE energy
AE cumulative energy
Precursor point
Engineering Stress (MPa)
AE energy (mV·ms)
AE cumulative energy (mV·ms)
Time (s)
(c)
3×10⁻⁵ s⁻¹
AE energy
AE cumulative energy
Precursor point
Engineering Stress (MPa)
AE energy (mV·ms)
AE cumulative energy (mV·ms)
Time (s)
(d)
R^2 = 0.99
$E_{max} \sim \dot{\varepsilon}^{\lambda}$
λ = 0.41±0.06
E_{max} (mV·ms)
Strain rate (s^{-1})

Fig. 3

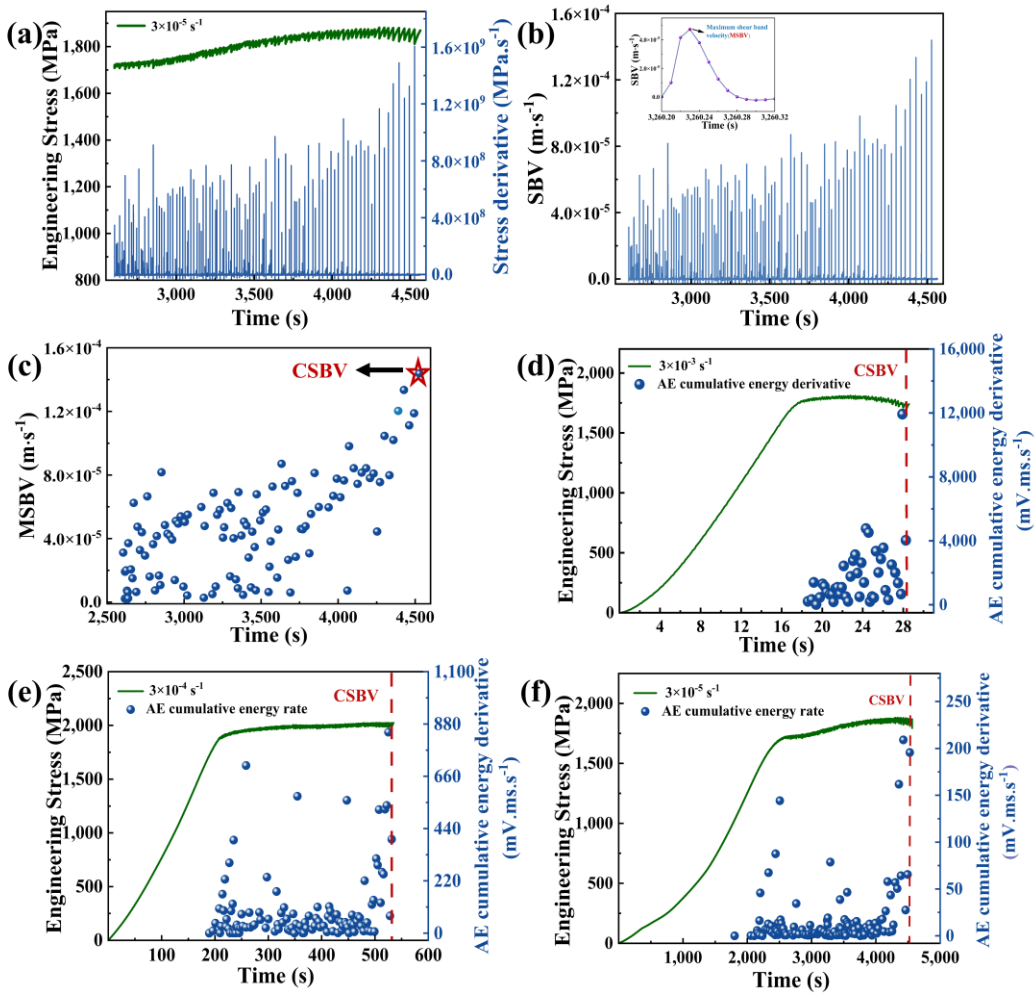
(a)
3×10⁻⁵ s⁻¹
Engineering Stress (MPa)
Stress derivative (MPa.s⁻¹)
Time (s)
(b)
SBV (m·s⁻¹)
Maximum shear band velocity(MSBV)
Time (s)
(c)
CSBV
MSBV (m·s⁻¹)
Time (s)
(d)
3×10⁻³ s⁻¹
AE cumulative energy derivative
CSBV
Engineering Stress (MPa)
AE cumulative energy derivative (mV.ms.s⁻¹)
Time (s)
(e)
3×10⁻⁴ s⁻¹
AE cumulative energy rate
CSBV
Engineering Stress (MPa)
AE cumulative energy derivative (mV.ms.s⁻¹)
Time (s)
(f)
3×10⁻⁵ s⁻¹
AE cumulative energy rate
CSBV
Engineering Stress (MPa)
AE cumulative energy derivative (mV.ms.s⁻¹)
Time (s)

Fig. 4

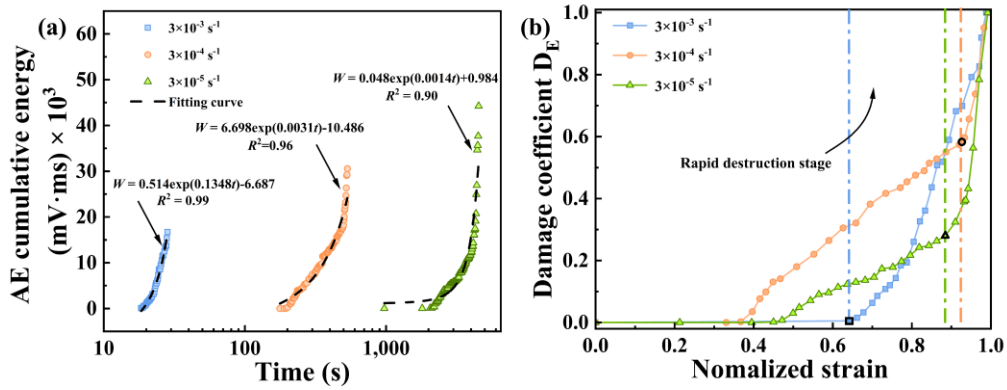
(a)
AE cumulative energy (mV·ms) × 10³
Time (s)
3×10⁻³ s⁻¹
3×10⁻⁴ s⁻¹
3×10⁻⁵ s⁻¹
Fitting curve
W = 0.514exp(0.1348t)-6.687
R² = 0.99
W = 6.698exp(0.0031t)-10.486
R²=0.96
W = 0.048exp(0.0014t)+0.984
R² = 0.90
(b)
Damage coefficient D_E
Nomalized strain
Rapid destruction stage

Fig. 5

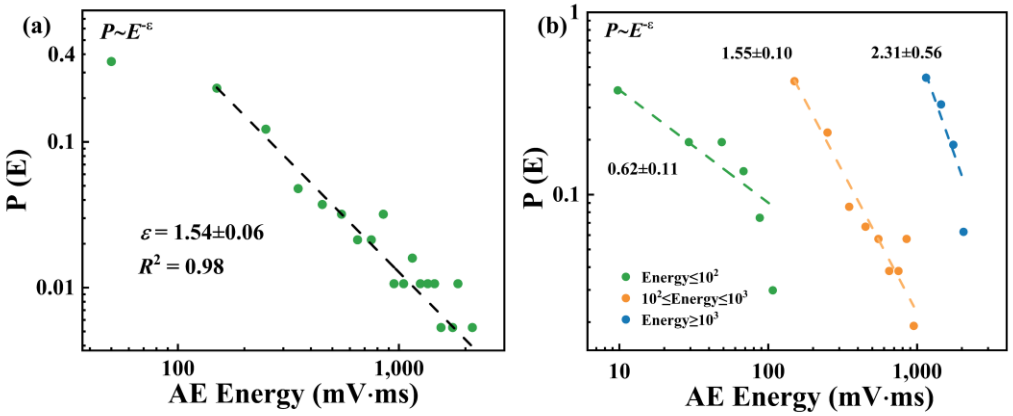
(a)
P~E^-ε
P (E)
AE Energy (mV·ms)
ε = 1.54±0.06
R² = 0.98
(b)
P~E^-ε
1.55±0.10
2.31±0.56
0.62±0.11
Energy≤10²
10²≤Energy≤10³
Energy≥10³

Fig. 6

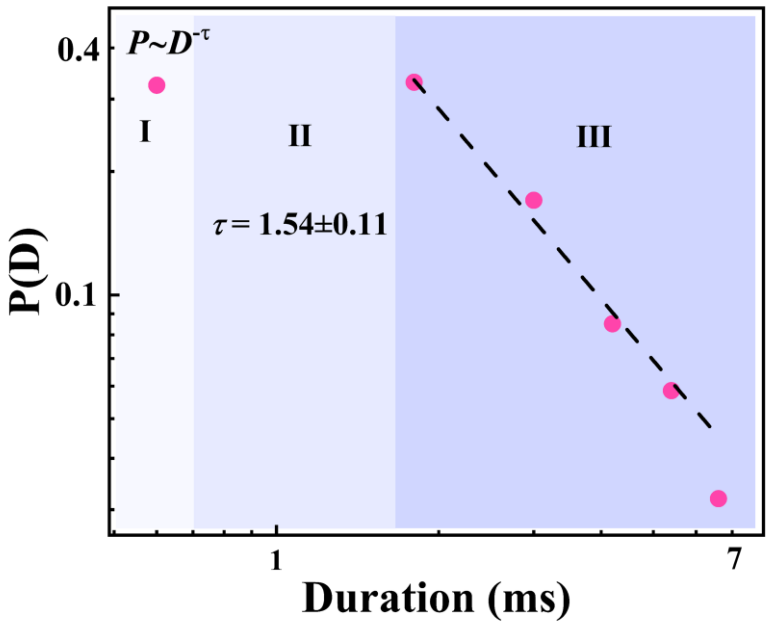
P~D^-τ
0.4
0.1
P(D)
I
II
III
τ = 1.54±0.11
1
7
Duration (ms)

Fig. 7

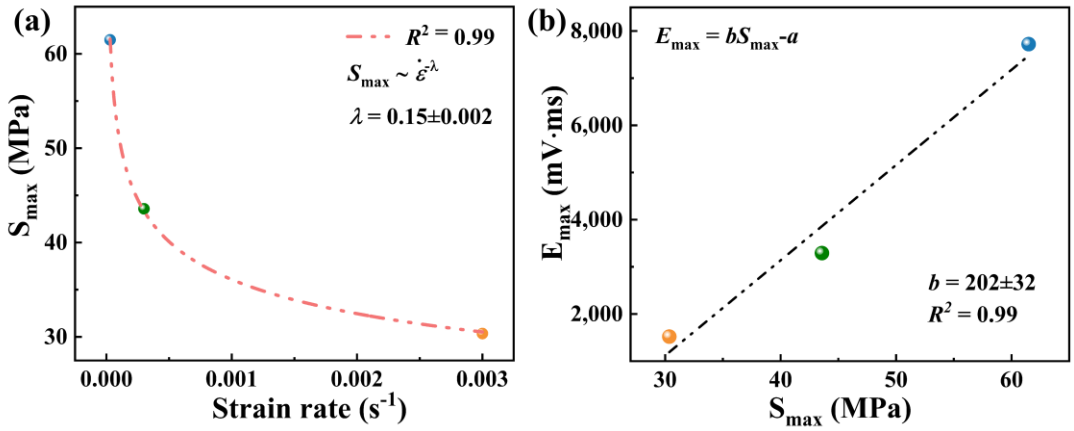
(a)
R² = 0.99
S_max ~ ε̇^λ
λ = 0.15±0.002
S_max (MPa)
60
50
40
30
0.000
0.001
0.002
0.003
Strain rate (s^-1)
(b)
E_max = bS_max-a
E_max (mV·ms)
8,000
6,000
4,000
2,000
b = 202±32
R² = 0.99
30
40
50
60
S_max (MPa)

Fig. 8

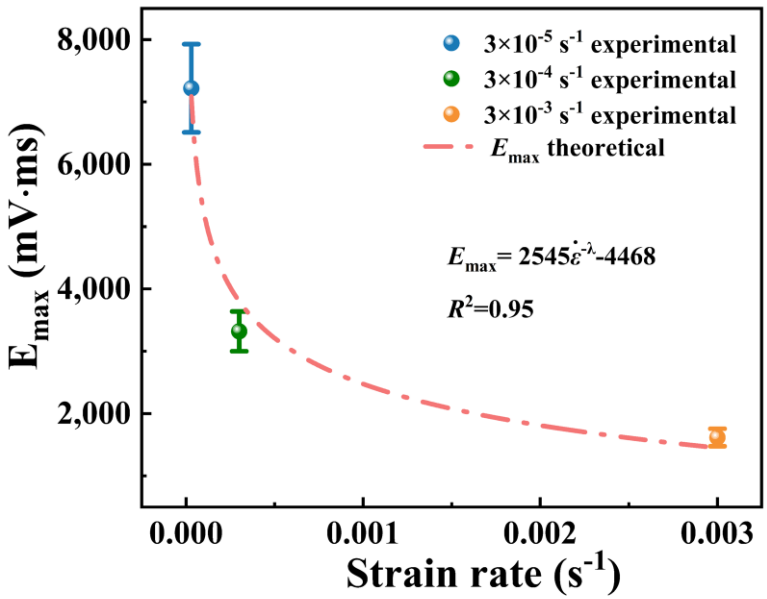
8,000
6,000
4,000
2,000
E_{max} (mV·ms)
0.000
0.001
0.002
0.003
Strain rate (s^{-1})
3×10^{-5} s^{-1} experimental
3×10^{-4} s^{-1} experimental
3×10^{-3} s^{-1} experimental
E_{max} theoretical
$E_{max}= 2545\dot{\varepsilon}^{-\lambda}-4468$
$R^2=0.95$

Table 2

	AE	CSBV	Failure
3×10^{-3} s^{-1}	8.35%	8.45%	8.55%
3×10^{-4} s^{-1}	15.76%	15.94%	16.05%
3×10^{-5} s^{-1}	13.28%	13.58%	13.69%

Table 2

Material	ε	Ref.
Coal	1.32	**[15]**
Sandstone	1.55	**[56]**
Calcareous sand	1.40	**[63]**
Prefabricated void siltstone	1.54	**[64]**
Vycor glass	1.40	**[65]**

References

[1] W. Klement, R.H. Willens, P. Duwez, Non-crystalline Structure in Solidified Gold–Silicon Alloys, Nature, 187 (1960) 869-870, http://dx.doi.org/10.1038/187869b0.

[2] M. Ashby, A. Greer, Metallic glasses as structural materials, Scr. Mater., 54 (2006) 321-326, http://dx.doi.org/10.1016/j.scriptamat.2005.09.051.

[3] M. Telford, The case for bulk metallic glass, Mater. Today, 7 (2004) 36-43, http://dx.doi.org/10.1016/s1369-7021(04)00124-5.

[4] C. Schuh, T. Hufnagel, U. Ramamurty, Mechanical behavior of amorphous alloys, Acta Mater, 55 (2007) 4067-4109, http://dx.doi.org/10.1016/j.actamat.2007.01.052.

[5] W.H. Wang, C. Dong, C.H. Shek, Bulk metallic glasses, Mater. Sci. Eng.: R: Rep., 44 (2004) 45-89, http://dx.doi.org/10.1016/j.mser.2004.03.001.

[6] J.F. Löffler, Bulk metallic glasses, Intermetallics, 11 (2003) 529-540, http://dx.doi.org/10.1016/s0966-9795(03)00046-3.

[7] S.Y. Liang, L.T. Zhang, Y.J. Wang, B. Wang, J.M. Pelletier, J.C. Qiao, A model on the coupling between cyclic fatigue and microstructure evolution in a metallic glass, Int J Fatigue., 187 (2024), http://dx.doi.org/10.1016/j.ijfatigue.2024.108446.

[8] J.W. Qiao, H.L. Jia, Y. Zhang, P.K. Liaw, L.F. Li, Multi-step shear banding for bulk metallic glasses at ambient and cryogenic temperatures, Mater. Chem. Phys., 136 (2012) 75-79, http://dx.doi.org/10.1016/j.matchemphys.2012.06.033.

[9] M.L. Falk, J.S. Langer, Dynamics of viscoplastic deformation in amorphous solids, Phys Rev E, 57 (1998) 7192-7205, http://dx.doi.org/10.1103/PhysRevE.57.7192.

[10] W.J. Wright, R. Saha, W.D. Nix, Deformation Mechanisms of the Zr40Ti14Ni10Cu12Be24 Bulk Metallic Glass, Mater. Trans., 42 (2001) 642-649, http://dx.doi.org/10.2320/matertrans.42.642.

[11] F.H. Dalla Torre, A. Dubach, M.E. Siegrist, J.F. Löffler, Negative strain rate sensitivity in bulk metallic glass and its similarities with the dynamic strain aging effect during deformation, Appl. Phys. Lett., 89 (2006) 091918-091921, http://dx.doi.org/10.1063/1.2234309.

[12] J.W. Qiao, Z. Wang, Z.M. Jiao, H.J. Yang, S.G. Ma, Z.H. Wang, B.S. Xu, Predicting Burst Sizes in Amorphous Alloys During Plastic Flows, Mat Sci Eng A-Struct, 609 (2014) 222-225, http://dx.doi.org/10.1016/j.msea.2014.05.009.

[13] Y.S. Luo, Z. Wang, J. Eckert, J.W. Qiao, A universal criterion for the failure threshold in slowly sheared bulk metallic glasses, J. Appl. Phys., 129 (2021) 155109-155115, http://dx.doi.org/10.1063/5.0044880.

[14] N. Zreihan, E. Faran, E. Vives, A. Planes, D. Shilo, Relations between stress drops and acoustic emission measured during mechanical loading, Physical Review Mater, 3 (2019) 043603-043611, http://dx.doi.org/10.1103/PhysRevMaterials.3.043603.

[15] X. Jiang, D. Jiang, J. Chen, E.K.H. Salje, Collapsing minerals: Crackling noise of sandstone and coal, and the predictability of mining accidents, Am. Mineral., 101 (2016) 2751-2758, http://dx.doi.org/10.2138/am-2016-5809CCBY.

[16] D. Jiang, K. Xie, J. Chen, S. Zhang, W.N. Tiedeu, Y. Xiao, X. Jiang, Experimental Analysis of Sandstone Under Uniaxial Cyclic Loading Through Acoustic Emission Statistics, Pure Appl. Geophys., 176 (2018) 265-277, http://dx.doi.org/10.1007/s00024-018-1960-4.

[17] B. Sun, S. Hou, J. Xie, S. Zeng, Failure Prediction of Two Types of Rocks Based on Acoustic Emission Characteristics, Adv. Civ. Eng., 2019 (2019) 5028489-5028500,

http://dx.doi.org/10.1155/2019/5028489.
[18] Z. Zhang, Z. Song, J. Lai, J. Qiu, Y. Cheng, J. Zhang, Critical slowing down precursor information for the acoustic emission response characteristics of defective tuffs, Theor. Appl. Fract. Mech., 129 (2024) 104220-104235, http://dx.doi.org/10.1016/j.tafmec.2023.104220.
[19] F. Spaepen, A MICROSCOPIC MECHANISM FOR STEADY STATE INHOMOGENEOUS FLOW IN METALLIC GLASSES, Acta Metall, 25 (1977) 407-415, http://dx.doi.org/10.1016/0001-6160(77)90232-2.
[20] A.S. Argon, PLASTIC DEFORMATION IN METALLIC GLASSES, Acta Metall, 27 (1978) 47-58, http://dx.doi.org/10.1016/0001-6160(79)90055-5.
[21] K.A. Dahmen, Y. Ben-Zion, J.T. Uhl, Micromechanical Model for Deformation in Solids with Universal Predictions for Stress-Strain Curves and Slip Avalanches, Phys Rev Lett, 102 (2009) 175501-175505, http://dx.doi.org/10.1103/PhysRevLett.102.175501.
[22] H.S. Chen, PLASTIC FLOW IN METALLIC GLASSES UNDER COMPRESSION, Scripta Metall, 7 (1973) 931-936, http://dx.doi.org/10.1016/0036-9748(73)90143-9.
[23] T. Mukaia, T.G. Niehb, Y. Kawamurac, A. Inoued, K. Higashi, Effect of strain rate on compressive behavior of a Pd40Ni40P20 bulk metallic glass, Intermetallics, 10 (2002) 1071–1077, http://dx.doi.org/10.1016/s0966-9795(02)00137-1.
[24] R. Maaß, J.F. Löffler, Shear-Band Dynamics in Metallic Glasses, Adv. Funct. Mater., 25 (2015) 2353-2368, http://dx.doi.org/10.1002/adfm.201404223.
[25] A. Vinogradov, A. Danyuk, V.A. Khonik, Localized and homogeneous plastic flow in bulk glassy Pd40Cu30Ni10P20: An acoustic emission study, J. Appl. Phys., 113 (2013) 153503-153511, http://dx.doi.org/10.1063/1.4801876.
[26] A. Lazarev, A. Vinogradov, S. Hashimoto, Comparative analysis of inhomogeneous plastic flow in bulk and ribbon metallic glasses monitored by acoustic emission, J. Alloys Compd., 504 (2010) S60-S64, http://dx.doi.org/10.1016/j.jallcom.2010.02.076.
[27] A. Vinogradov, A. Lazarev, D.V. Louzguine-Luzgin, Y. Yokoyama, S. Li, A.R. Yavari, A. Inoue, Propagation of shear bands in metallic glasses and transition from serrated to non-serrated plastic flow at low temperatures, Acta Mater, 58 (2010) 6736-6743, http://dx.doi.org/10.1016/j.actamat.2010.08.039.
[28] R. Čtvrtlík, J. Čech, J. Tomáštík, L. Václavek, P. Haušild, Plastic instabilities explored via acoustic emission during spherical nanoindentation, Mat Sci Eng A-Struct, 841 (2022) 143019-143031, http://dx.doi.org/10.1016/j.msea.2022.143019.
[29] A. Vinogradov, On shear band velocity and the detectability of acoustic emission in metallic glasses, Scr. Mater., 63 (2010) 89-92, http://dx.doi.org/10.1016/j.scriptamat.2010.03.023.
[30] B.A. Sun, Y. Yang, W.H. Wang, C.T. Liu, The Critical Criterion on Runaway Shear Banding in Metallic Glasses, Sci. Rep., 6 (2016) 21388-21398, http://dx.doi.org/10.1038/srep21388.
[31] J. Geng, L. Cao, Failure analysis of water-bearing sandstone using acoustic emission and energy dissipation, Eng. Fract. Mech., 231 (2020) 107021-107031, http://dx.doi.org/10.1016/j.engfracmech.2020.107021.
[32] P. Thurnheer, R. Maaß, K.J. Laws, S. Pogatscher, J.F. Löffler, Dynamic properties of major shear bands in Zr–Cu–Al bulk metallic glasses, Acta Mater, 96 (2015) 428-436, http://dx.doi.org/10.1016/j.actamat.2015.05.028.
[33] D. Klaumünzer, R. Maaß, J.F. Löffler, Stick-slip dynamics and recent insights into shear banding in metallic glasses, J. Mater. Res., 26 (2011) 1453-1463, http://dx.doi.org/10.1557/jmr.2011.178.

[34] F. Yang, Plastic flow in bulk metallic glasses: Effect of strain rate, Appl. Phys. Lett., 91 (2007), http://dx.doi.org/10.1063/1.2768029.

[35] Y.Q. Cheng, Z. Han, Y. Li, E. Ma, Cold versus hot shear banding in bulk metallic glass, Phys Rev B, 80 (2009) 134115-134121, http://dx.doi.org/10.1103/PhysRevB.80.134115.

[36] S.X. Song, H. Bei, J. Wadsworth, T.G. Nieh, Flow serration in a Zr-based bulk metallic glass in compression at low strain rates, Intermetallics, 16 (2008) 813-818, http://dx.doi.org/10.1016/j.intermet.2008.03.007.

[37] W.H. Jiang, G.J. Fan, F.X. Liu, G.Y. Wang, H. Choo, P.K. Liaw, Spatiotemporally inhomogeneous plastic flow of a bulk-metallic glass, Int. J. Plast., 24 (2008) 1-16, http://dx.doi.org/10.1016/j.ijplas.2007.01.015.

[38] B.A. Sun, S. Pauly, J. Hu, W.H. Wang, U. Kühn, J. Eckert, Origin of Intermittent Plastic Flow and Instability of Shear Band Sliding in Bulk Metallic Glasses, Phys Rev Lett, 110 (2013) 225501-225506, http://dx.doi.org/10.1103/PhysRevLett.110.225501.

[39] B.A. Sun, S. Pauly, J. Tan, M. Stoica, W.H. Wang, U. Kühn, J. Eckert, Serrated flow and stick–slip deformation dynamics in the presence of shear-band interactions for a Zr-based metallic glass, Acta Mater, 60 (2012) 4160-4171, http://dx.doi.org/10.1016/j.actamat.2012.04.013.

[40] J.J. Li, Z. Wang, J.W. Qiao, Power-law scaling between mean stress drops and strain rates in bulk metallic glasses, Materials & Design, 99 (2016) 427-432, http://dx.doi.org/10.1016/j.matdes.2016.03.092.

[41] B.A. Sun, H.B. Yu, W. Jiao, H.Y. Bai, D.Q. Zhao, W.H. Wang, Plasticity of Ductile Metallic Glasses: A Self-Organized Critical State, Phys Rev Lett, 105 (2010) 035501-035505, http://dx.doi.org/10.1103/PhysRevLett.105.035501.

[42] F.F. Wu, W. Zheng, S.D. Wu, Z.F. Zhang, J. Shen, Shear stability of metallic glasses, Int. J. Plast., 27 (2011) 560-575, http://dx.doi.org/10.1016/j.ijplas.2010.08.004.

[43] Y. Xue, L. Wang, X. Cheng, F. Wang, H. Cheng, H. Zhang, A. Wang, Strain rate dependent plastic mutation in a bulk metallic glass under compression, Mater. Des., 36 (2012) 284-288, http://dx.doi.org/10.1016/j.matdes.2011.11.025.

[44] J. Hu, B.A. Sun, Y. Yang, C.T. Liu, S. Pauly, Y.X. Weng, J. Eckert, Intrinsic versus extrinsic effects on serrated flow of bulk metallic glasses, Intermetallics, 66 (2015) 31-39, http://dx.doi.org/10.1016/j.intermet.2015.06.018.

[45] Y. Chen, M.Q. Jiang, L.H. Dai, Collective evolution dynamics of multiple shear bands in bulk metallic glasses, Int. J. Plast., 50 (2013) 18-36, http://dx.doi.org/10.1016/j.ijplas.2013.03.010.

[46] J.G. Wang, Y. Pan, S.X. Song, B.A. Sun, G. Wang, Q.J. Zhai, K.C. Chan, W.H. Wang, How hot is a shear band in a metallic glass?, Mat Sci Eng A-Struct, 651 (2016) 321-331, http://dx.doi.org/10.1016/j.msea.2015.10.125.

[47] W. He, C. Huang, H. Chen, P. Zhu, Study on Acoustic Emission Characteristics and Damage Evolution Law of Red Sandstones under Different Loading Rates, IOP Conf. Ser.: Earth Environ. Sci, 861 (2021) 042080-042089, http://dx.doi.org/10.1088/1755-1315/861/4/042080.

[48] L.M. Kachanov, Time of the Rupture Process under Creep Conditions, Izy Akad, Nank S. S. R. Otd Tech Nauk, 8 (1958) 26-31,

[49] J. Antonaglia, X. Xie, G. Schwarz, M. Wraith, J. Qiao, Y. Zhang, P.K. Liaw, J.T. Uhl, K.A. Dahmen, Tuned Critical Avalanche Scaling in Bulk Metallic Glasses, Sci. Rep., 4 (2014) 04382-04387, http://dx.doi.org/10.1038/srep04382.

[50] E.K.H. Salje, K.A. Dahmen, Crackling Noise in Disordered Materials, Annu. Rev. Condens. Matter

Phys., 5 (2014) 233-254, http://dx.doi.org/10.1146/annurev-conmatphys-031113-133838.

[51] M.C. Gallardo, J. Manchado, F.J. Romero, J. del Cerro, E.K.H. Salje, A. Planes, E. Vives, R. Romero, M. Stipcich, Avalanche criticality in the martensitic transition of Cu67.64Zn16.71Al15.65shape-memory alloy: A calorimetric and acoustic emission study, Phys Rev B, 81 (2010) 174102-174110, http://dx.doi.org/10.1103/PhysRevB.81.174102.

[52] B.-a. Sun, C.-t. Liu, Y. Yang, Rate Dependence of Serrated Flow and Its Effect on Shear Stability of Bulk Metallic Glasses, J IRON STEEL RES INT, 23 (2016) 24-30, http://dx.doi.org/10.1016/s1006-706x(16)30006-1.

[53] j.j. Li, j.w. Qiao, K.A. Dahmen, W.m. Yang, B.l. Shen, M.w. Chen, Universality of slip av alanches in a ductil e F e-based bulk m etallic glass, J IRON STEEL RES INT, 24 (2017) 366-371, http://dx.doi.org/10.1016/S1006-706X(17)30054-7.

[54] L. Hanlong, J. Linsen, J. Deyi, X. Kainan, J. Xiang, Experimental and maximum likelihood theory on acoustic emission statistic effect of coal-sandstone composite rock, J. China Coal Soc., 44 (2019) 1544-1551, http://dx.doi.org/10.13225/j.cnki.jccs.2018.0785.

[55] R. Sarmah, G. Ananthakrishna, B.A. Sun, W.H. Wang, Hidden order in serrated flow of metallic glasses, Acta Mater, 59 (2011) 4482-4493, http://dx.doi.org/10.1016/j.actamat.2011.03.071.

[56] G.F. Nataf, P.O. Castillo-Villa, J. Baró, X. Illa, E. Vives, A. Planes, E.K.H. Salje, Avalanches in compressed porousSiO2-based materials, Phys Rev E, 90 (2014) 022405-022414, http://dx.doi.org/10.1103/PhysRevE.90.022405.

[57] K.A. Dahmen, Y. Ben-Zion, J.T. Uhl, A simple analytic theory for the statistics of avalanches in sheared granular materials, Nature Physics, 7 (2011) 554-557, http://dx.doi.org/10.1038/nphys1957.

[58] Y. Zhao, H. Liu, K. Xie, E.K.H. Salje, X. Jiang, Avalanches in Compressed Sandstone: Crackling Noise under Confinement, Crystals, 9 (2019) 582-592, http://dx.doi.org/10.3390/cryst9110582.

[59] E.K.H. Salje, H. Liu, L. Jin, D. Jiang, Y. Xiao, X. Jiang, Intermittent flow under constant forcing: Acoustic emission from creep avalanches, Appl. Phys. Lett., 112 (2018) 054101-054106, http://dx.doi.org/10.1063/1.5018137.

[60] Y. Chen, K. Tang, B. Gou, F. Jiang, X. Ding, E.K.H. Salje, Acoustic emission spectra and statistics of dislocation movements in Fe40Mn40Co10Cr10 high entropy alloys, J. Appl. Phys., 132 (2022), http://dx.doi.org/10.1063/5.0098813.

[61] B. Yuan, j.j. Li, j.w. Qiao, Statistical analysis on strain-rate effects during serrations In a Zr-based bulk metallic glass, J IRON STEEL RES INT, 24 (2017) 455-461, http://dx.doi.org/10.1016/S1006-706X(17)30069-9.

[62] A. Yonezu, X. Chen, Micro-scale damage characterization in porous ceramics by an acoustic emission technique, CERAM INT, 40 (2014) 9859-9866, http://dx.doi.org/10.1016/j.ceramint.2014.02.079.

[63] W. Lei, J. Xiang, X. Yang, W. Huan-rang, S. Jun-jie, L. Han-long, Y. Zhi-hua, Experimental research on size effect and avalanche dynamics characteristics of calcareous sand particles, Chin. J. Geotech. Eng., 43 (2021) 1029-1038, http://dx.doi.org/10.11779/CJGE202106006.

[64] X. Liu, L. Zheng, H. He, Q. Qiu, Z. Liu, X. Li, L. Yan, G. Huang, Z. Wen, Characterization of Acoustic Emission Parameters during Fracture Process of Siltstone with Prefabricated Void, Geofluids, 2022 (2022) 6188833-6188842, http://dx.doi.org/10.1155/2022/6188833.

[65] J. Baró, Á. Corral, X. Illa, A. Planes, E.K.H. Salje, W. Schranz, D.E. Soto-Parra, E. Vives, Statistical Similarity between the Compression of a Porous Material and Earthquakes, Phys Rev Lett, 110 (2013) 088702-088707, http://dx.doi.org/10.1103/PhysRevLett.110.088702.